



Mesoporous TiO₂ Monoliths Impregnated with CdS and CuO Nanoparticles for Airborne Bacteria Inactivation Under Visible Light

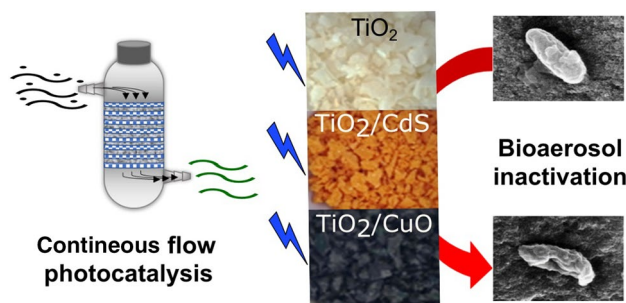
Armin Hernández-Gordillo¹ · Sonia Arriaga¹

Received: 25 February 2021 / Accepted: 10 May 2021 / Published online: 23 May 2021
© The Author(s), under exclusive licence to Springer Science+Business Media, LLC, part of Springer Nature 2021

Abstract

In this work, macroscopic TiO₂ monoliths are proposed to serve simultaneously as support and co-catalyst in a continuous flow photoreactor. The impregnation via one-pot of mesoporous TiO₂ with CdS (m-TiO₂/CdS) and CuO (m-TiO₂/CuO) nanoparticles enabled the formation of photocatalytic heterojunctions retaining high specific surface area (~ 100 m²/g). The impregnated monoliths of 2–3 mm in size were employed as photocatalysts to inactivate airborne bacteria under blue light, reducing the emission of living airborne bacteria up to 0.1% and 37.7% when using m-TiO₂/CdS and m-TiO₂/CuO, respectively. Bacteria were characterized and quantified by flow cytometry and cell lysis was confirmed by SEM, detecting collapsed bacteria. Along 96 h of continuous photocatalysis at a flow rate of 2.2 L/min, the cell concentration presented maxima and minima due to the adsorption–desorption stages of bioaerosols over the catalysts, in concordance with thermal gravimetric analysis. The reactivation of catalysts was achieved by calcination at 400 °C, however, after a third re-cycle, the photocatalytic activity for all monoliths was practically negligible because the physicochemical surface changes hinder the adequate bioaerosol adsorption. These porous systems could emerge as promising gas-phase catalysts since the mass transport is facilitated by porosity and the release of catalyst nanoparticles is avoided by the active support, providing a safe and viable model for bioaerosols inactivation to improve indoor air quality with the use of interior lighting.

Graphic abstract



Keywords Photocatalysis · Visible-light-driven · TiO₂ monolith · CdS and CuO nanoparticles · Airborne bacteria

1 Introduction

Air pollution is a global problem, whose impact on human health is increasingly evident. Poor air quality has been linked to premature death, chronic diseases, low IQ, decrease in labor productivity, among other adverse conditions [1, 2]. Air pollutants include carbon, nitrogen, and sulfur oxides; ozone; particulate matter (PM_{2.5}, PM₁₀); volatile organic

✉ Sonia Arriaga
sonia@ipicyt.edu.mx

¹ División de Ciencias Ambientales, Instituto Potosino de Investigación Científica y Tecnológica (IPICYT), Camino a la Presa San José 2055, 78216 San Luis Potosí, México

compounds (VOCs), and bioaerosols (fungi, bacteria, viruses, genetic material, etc.) [3, 4].

Commonly, bioaerosols concentrations in indoor environments poorly ventilated are a real threat to exposed individuals, even, the artificial ventilation systems become reservoirs of microorganisms when they are not cleaned and disinfected adequately [5, 6]. Exposure to bioaerosol causes adverse effects on health, such as infectious diseases, acute toxic effects, and allergies. For example, diseases like COVID-19 are highly infectious because the virus SARS-CoV-2 is broadly spread in the aerosols principally in enclosed spaces [7, 8]. Thus, the urgency of methods for preventing the harmful effects of bioaerosols has been evidenced, pointing out in recirculation and purification processes to improve indoor air quality.

Among the most appropriate techniques for the removal of biological particles, advanced oxidation processes (AOPs) have shown a great effectivity since they can simultaneously capture and irreversibly transform bioaerosols into inert compounds [9–11]. Photocatalytic processes using AOPs, generally promoted by reusable nanometric semiconductors, have been broadly applied to inactivate microorganisms in liquid phase [12, 13]. On the contrary, the inactivation of bioaerosols is scarcely studied due to the technical difficulties in bioaerosol sampling and characterization [14–16]. A continuous flow in photocatalytic systems (e.g. air circulation) hampers the use of powders as catalysts because of the undesired dispersion in the flow, as an alternative to avoid catalysts loss in continuous flow air disinfection systems, the impregnation of nanoparticles on materials with macroscopic sizes has been employed [17–21]. However, the reuse of impregnated materials is not always possible because the supports are not as durable as the catalysts. For this reason, support materials based on ceramic monoliths have been proposed as macroscopic support to avoid the dragging out catalysts with the airflow in the case of reactors for air purification [22, 23]. In particular, titanium dioxide can be synthesized in a wide range of sizes according to the characteristics required resulting in suitable support for catalytic nanoparticles [24, 25]. In addition to its photocatalytic power, the choice of TiO₂ as support is based on the high thermal and mechanical stability, as well as the facility and low cost of synthesis [26]. Thus, a porous monolith of TiO₂ could be ideal in the air purification processes, since it meets the requirement of having a macroscopic particle size, without losing impregnation capacity because of its porosity (high specific surface area) [27–29].

Loading TiO₂ with a semiconductor with a bandgap lower than 3.1 eV improves the energy transference of the irradiated energy which resulted in an increase in the photocatalytic efficiency under visible light [30–33]. For example, CdS/TiO₂ and CuO/TiO₂ heterostructures have been successfully applied for microbial degradation under visible

light in aqueous systems [34–38]. However, the application of these heterogeneous photocatalysts for indoor air purification remains unexplored despite the possibility of exploiting the inherent interiors lighting to produce the AOPs. This is probably because continuous flow systems present a great challenge for the design of photocatalytic reactors since the increase in the number of variables to be considered, such as humidity, flow rate, pressure, catalyst load, etc. [39, 40].

In the present work, nanoparticles of CdS and CuO supported on a porous TiO₂ medium were synthesized in order to improve their reactivity due to the cooperative phenomena of both semiconductors. The modification of the TiO₂ surface by integrating CuO or CdS was used successfully for the removal and inactivation of airborne bacteria under visible light irradiation. Therefore, the porous TiO₂ support acts as both an adsorbent and a co-catalyst, allowing the enhancement of airborne-solid interactions and the overall photocatalytic process. The characterization of airborne bacteria was performed using flow cytometry as an alternative to culture-dependent methods since they can quantify the total concentration of cells and metabolites [41, 42]. Flow cytometry enabled a rapid and accurate measurement of biological species in air samples in a short time, resulting in a powerful tool for indoor air quality management. These porous supports facilitate the study of various combinations of loaded nanoparticles, which contributes to a better design of high-performance catalysts for the filtration-inactivation of future air treatment technologies by using indoor illumination.

2 Materials and Methods

2.1 Materials

Titanium isopropoxide (Ti(iPrO)₄), PEG 10,000 (MW 10,000 g/mol) and ethyl acetylacetonate (EtAcAc) were supplied by Sigma-Aldrich. Isopropanol, ammonium nitrate, absolute ethanol, cadmium nitrate, copper sulfate, thiourea (Meyer). Sterile counting beads (BD Medical Technology) were used for microorganism quantification. Thiazole orange and propidium iodide were used as fluorochromes (Sigma-Aldrich). PBS (phosphate-buffered saline) at pH 7.2 was prepared. All reagents were used as received. Distilled water was used in all experiments.

2.2 Photocatalysts Synthesis

The synthesis of mesoporous TiO₂ monoliths (m-TiO₂), based on the sol-gel method, was performed following the procedure described by Hasegawa [43]. In a typical reaction, 100 mL of Ti(iPrO)₄, 50 mL of isopropanol, and 50 mL of EtAcAc were mixed. The solution was heated to 60 °C and 6.0 g of PEG 10,000 were completely dissolved. The

solution was cooled at 40 °C, 20 mL of ammonium nitrate 1.0 M was added with vigorous stirring and aged at 60 °C, 24 h. The solvent exchange at 60 °C was achieved using 100 mL of water/ethanol (30/70, 50/50, and 70/30) changing the solution after 24 h, and subsequently, the addition of pure water to ensure the complete hydrolysis of EtAcAc and condensation of Ti(iPrO)₄. Then, monoliths were dried at 80 °C (24 h) and calcined (400 °C, 1 °C/min, 2 h). For the synthesis of impregnated monoliths, nanoparticles of CdS or CuO suspended in 10 mL of isopropanol were added after PEG dissolution, all successive steps in the protocol were identical. To synthesize the CdS nanoparticles, an aqueous solution of cadmium nitrate and thiourea (molar ratio 1:2) was adjusted to pH 8 with NaOH, the mixture was heated at 150 °C, 20 min in a microwave digester (ETHOS UP, Milestone). The CdS was recovered by centrifugation, washed three times with water, and calcined at 200 °C, 2 h. The CuO nanoparticles were synthesized from a solution of copper sulfate, pH 10, heated with vigorous stirring at 80 °C, 30 min. The brown solution was centrifuged (5000 rpm, 5 min), washed three times with water, and calcined at 200 °C, 2 h. The reactivation of catalysts was achieved by calcination at 400 °C, 1 °C/min, 2 h.

Crystallinity was analyzed using a Bruker Advance 8 X-ray diffractometer (CuK_α, 1.5404 Å), a step size of 0.01°. The crystallite size was estimated by applying the Scherrer equation (Scherrer constant K = 0.9) using the diffraction peak of planes (101) and (110) of anatase and wurtzite, respectively. Nitrogen adsorption/desorption measurements at 77 K were performed on an ASAP 2020 (Micromeritics) volumetric adsorption analyzer; before the measurements, the samples were outgassed. The specific surface area of solid samples was calculated by the multiple-point Brunauer–Emmett–Teller (BET) method in the relative pressure range of P/P₀ = 0.05–0.25. Pore size distribution curves were computed using the non-local density functional theory (NLDFT) method (using the nitrogen desorption branch, assuming cylindrical pores on silica). Visible diffuse-reflectance spectra (UV–vis DRS) were measured on Cary 500 UV–Vis spectrophotometer (PE, USA). Bandgap

was calculated using the Tauc plot according to the equation $\alpha h\nu = A(h\nu - E_g)^{n/2}$ where α , $h\nu$, A , and E_g correspond to the absorption coefficient, photon energy, a constant, and bandgap of semiconductor, respectively. For indirect transitions (m-TiO₂ and m-TiO₂/CdS) $n = 4$ and for a direct semiconductor $n = 1$ (m-TiO₂/CuO) [44]. For DRX and UV–vis DRS analyses the monoliths were previously pulverized with a mortar and pestle.

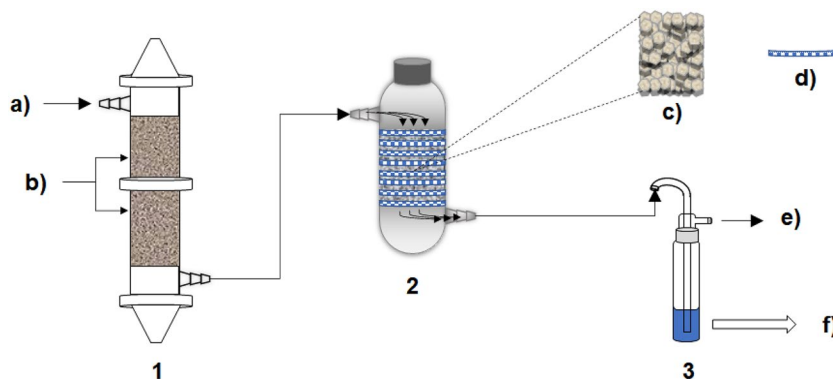
2.3 Airborne Bacteria and Photocatalytic System

A biofilter degrading toluene vapors was adopted as a bioaerosol emitter, whose outlet stream was connected to the photoreactor inlet. The biofilter, a two-module glass reactor (2 × 1.1 L), was packed with Perlite and inoculated with a consortium of activated sludge obtained from a wastewater treatment plant (San Luis Potosí, México). The photoreactor comprised an annular plug flow reactor with a working volume of 200 mL ($r = 2.5$ cm, $h = 10.2$ cm). A scheme of this set-up is given in Fig. 1. The reactor was packed with 25 g of monoliths (m-TiO₂, m-TiO₂/CuO, or m-TiO₂/CdS). A dark period was ensured by completely covering the photoreactor with aluminum foil. In the photolytic and photocatalytic steps, it was irradiated with 85 blue LEDs (2835, ShowLUX) around the photoreactor body (6.8 W, 340 lm, main radiation 460 nm). For the photolytic tests, the reactor remained empty (without catalyst) with a constant gas flow and a retention time of 6 s. Samples were collected for 6 h every 30 min.

2.4 Bioaerosols Sampling and Characterization

Bioaerosol sampling was carried out by liquid impingement as was described previously [41]. A glass impinger AGI-30 (Ace Glass, Inc., Vineland, USA) whose output was connected to a vacuum pump (Gast, No. DOA-P704A-AA) coupled with a rotameter for airflow regulation was used to sampling bioaerosols. The impinger was fed with a sonic flow of 12.5 Lmin⁻¹ for 30 min, consisting of the outlet flow of the reactors (2.2 Lmin⁻¹ air), and an ambient airline

Fig. 1 Schematic view of the continuous flow photocatalytic system. **1** biofilter, a) inlet, toluene/humid-air flow 2.2 L/min and b) activated sludge supported on perlite. **2** photoreactor comprised by c) packed monolithic catalyst and d) blue LED strip lights. **3** Impinger for air sampling, e) outlet flow, f) bioaerosols collected in PBS for characterization



(10.3 Lmin⁻¹ air) with a 0.45 μm hydrophilic glass fiber filter (Merck Millipore). Impingers containing 20 mL of PBS pH 7.2 were sterilized before sampling.

The characterization of bioaerosol in terms of cell viability and concentration was analyzed with a Flow Cytometer BD FACSCalibur (Model 342,975, USA). A volume of 500 μL of bioaerosol sample was stained, the optimal dye concentrations and incubation time were 5 μL of thiazole orange (2.0 μM) and 5 μL of propidium iodide (0.1 mM), for 10 min of staining. After incubation, 25 μL of counting beads fluorescent suspension (940 beads/μL, BD, 335,925) were added. Samples were measured after staining at a high flow rate up to reach 300–600 counts per second and 10,000 target cells were counted for the acquisition of the database, this acquisition was performed in triplicate. Cell Quest Pro software was used to scan the data.

To calculate the cell concentration in each liquid sample Eq. 1 was used.

$$\frac{Cell}{\mu L} = \frac{E_R V_b C_b}{V_{tot} E_b} \quad (1)$$

where E_R is the total events in the R region (corresponding to live, dead, or injured cells), V_b and C_b is the volume and concentration of the counting beads respectively, V_{tot} is the total volume of the sample and E_b is the total events of counting beads.

The concentration of bioaerosols in the air, according to the sampling methodology was calculated with the following equation:

$$\frac{Cell}{m^3} = \left(\frac{Cell}{\mu L} \right) \left(\frac{V_s}{Q * t} \right) \quad (2)$$

were V_s being the total volume of the liquid sample ($20.0 \times 10^3 \mu L$), Q the flow rate ($2.2 \times 10^{-3} m^3/min$), and t the sampling time (30 min).

Bioaerosols adsorbed on the TiO₂ monoliths were analyzed by SEM before and after the photocatalytic performance. The monoliths were submerged in a glutaraldehyde solution (4.0% in PBS) overnight at 4 °C, washed with PBS and water three times and twice, respectively. Samples were dehydrated by a graded series of ethanol (33% for 15 min, 66% for 15 min, 90% for 15 min, and twice 100% for 20 min). The samples were dried, gold sputter-coated, and visualized using a field emission scanning electron microscope (FEI Quanta 250).

Bioaerosol samples collected by impingers also contained all the material that was released from the photoreactor, then, spectrophotometric analysis of Cd, Cu, and Ti species was performed to monitor the release of the catalysts. UV–vis spectrum of 500 μL of each bioaerosols sample was measured in the range of 250 nm to 600 nm (path length, 1 cm). TiO₂ has an absorbance at ≤400 nm, while CdS and

CuO absorb in the visible region with molar absorptivity coefficients in the order of $10^6 M^{-1} cm^{-1}$ [45, 46].

3 Results and Discussion

3.1 Photocatalysts Characterization

Monoliths of pure mesoporous TiO₂ (m-TiO₂), CdS supported on mesoporous TiO₂ (m-TiO₂/CdS) and CuO supported on mesoporous TiO₂ (m-TiO₂/CuO) were synthesized with a particle size in the range of 2–3 μm. This grain size was adequate for packing the reactor and it avoided the loss of the catalysts in the continuous air flow. To ensure a high photocatalytic activity in the visible light radiation, the maximum load of nanoparticles was employed, this increases the total number of active sites on the surface. For the monoliths, the maximum percentage in weight of nanoparticles impregnated on m-TiO₂/CdS and m-TiO₂/CuO was 8.5% and 7.5%, respectively. Increasing these loads, the sol–gel process was heterogeneous resulting in precipitates. The synthesized monoliths were calcinated at 400 °C for 2 h. This low calcination temperature prevented the collapse of the mesoporous structure but it was enough to remove organic residues [47, 48]. After calcination, all monoliths have a crystalline structure corresponding to anatase (Fig. 2). In the case of m-TiO₂, the diffractions patterns correspond exclusively to pure anatase (Fig. 2a), the diffractogram of m-TiO₂/CdS shows anatase and wurtzite patterns (Fig. 2b) confirming the presence of crystalline CdS. The crystalline phases of CuO were not detected in m-TiO₂/CuO possibly due to the small load of CuO and overlapping with the broader diffraction peak of TiO₂ at 38° (principal peaks of CuO: 35.5°

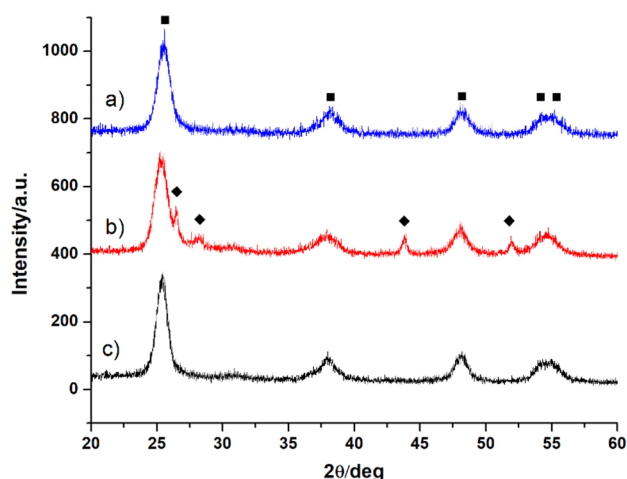


Fig. 2 X-ray diffraction patterns of a) m-TiO₂, b) m-TiO₂/CdS, and c) m-TiO₂/CuO. Squares and diamonds designate anatase (TiO₂) and wurtzite (CdS) patterns, respectively

and 38.7°) [49]. In all cases, analysis by energy-dispersive spectroscopy (EDS) confirmed the presence of the constituent elements of each synthesized monolith (Fig. S1).

The textural properties of monoliths were analyzed by nitrogen adsorption–desorption, the isotherms of the three materials are shown in Fig. 3a. The isotherms are of type IV with hysteresis loop type H2 correspond to a mesoporous structure with a mean pore size diameter of 8.1 nm. The specific surface area of m-TiO₂/CuO (113 m²/g) is slightly higher than m-TiO₂ and m-TiO₂/CdS (~100 m²/g) possibly due to the variation in the synthesis of each catalyst. These specific surface areas are superior compared to the most common TiO₂ catalyst, Degussa P25, which has a specific surface area of ~50 m²/g [50], and even greater than other reported TiO₂ monoliths

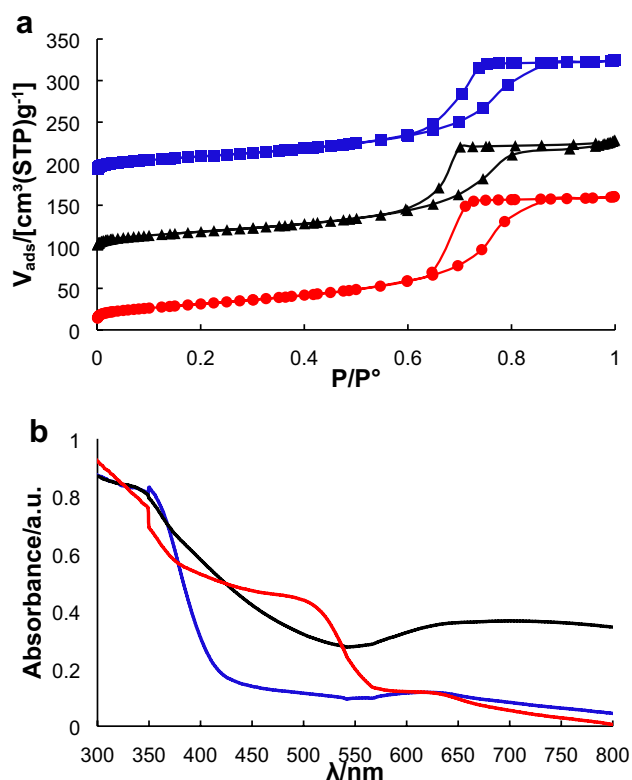


Fig. 3 **a** Nitrogen adsorption/desorption isotherms and **b** UV–visible diffuse reflectance spectra of m-TiO₂ (blue), m-TiO₂/CdS (black), and m-TiO₂/CuO (red)

Table 1 Physicochemical properties of the synthesized photocatalysts

Name	S_{BET} (m ² g ⁻¹)	$D_{p(NLDFT)}$ (nm)	Bandgap (eV)	$D_{Crystal}$ (nm)	ρ_a (gcm ⁻³)	L_{np} (%)
m-TiO ₂	104	8.1	3.1	8.5 (A)	1.3	0.0
m-TiO ₂ /CdS	102	8.1	2.2	6.8 (A), 20.1 (W)	1.2	8.5
m-TiO ₂ /CuO	113	8.1	1.4	8.1 (A)	1.2	7.5

S_{BET} BET specific surface area, $D_{p(NLDFT)}$ average pore diameter by NLDFT, $D_{Crystal}$ crystal diameter by Scherrer equation, (A) anatase phase, (W) wurtzite phase, ρ_a apparent density, L_{np} nanoparticle loading.

[26]. Furthermore, the monolith structure allowed the presence of macroporosity, therefore, it may have a high potential to be used as a material for air filtration. The UV–vis diffuse reflectance spectra of catalysts are shown in Fig. 3b. It can be seen that the absorption intensity of pure m-TiO₂ starts to increase at ~410 nm, indicating a bandgap of 3.1 eV. It can be clearly seen that the absorption range of m-TiO₂/CdS and m-TiO₂/CuO samples were extended to the visible region. For m-TiO₂/CuO, two closely spaced conduction bands formed by sharing interfacial O²⁻ entities between Cu²⁺ and Ti⁴⁺ were observed. The broad absorption band below 600 nm is associated with the d-d transition of Cu(II) and the weak absorption in the range of 600–800 nm is due to the intrinsic excitation band of CuO component and the d-d transition of Cu(II) species [51, 52]. Similarly, the diffuse reflectance spectrum of m-TiO₂/CdS showed a synergistic effect between CdS nanoparticles and TiO₂ mesoporous support which resulted in a high absorption capacity in the visible region [53].

Table 1 summarizes the physicochemical characteristics of the three catalysts. According to the similar textural parameters (pore size diameter and specific surface area), the photocatalytic performance can be attributed directly to the composition and electronic structure of the materials, as is discussed below.

The macroscopic aspect of the monoliths is shown in Figs. 4a–c, the color of impregnated TiO₂ is preserved from the original nanoparticles. The microscopic morphology of monoliths is rugged due to the porosity of TiO₂ (Figs. 4d–f), nanoparticles of CdS and CuO incrustated on the surface were present along with the entire exposed faces of the monoliths. The methodology of impregnation was made using the sol–gel technique, which is useful to ensure the retention of nanoparticles on the surface of the support. Nanoparticles retention on monoliths was tested under air flow as is discussed below.

3.2 Airborne Bacteria Inactivation by Photocatalysis under Visible Light

In this work, a biofilter was used as a constant source of bio-aerosols [54]. Details about the operation of the biofilter in steady-state can be found at S2.

To differentiate living, dead, and injured bacteria in flow cytometry, it was used thiazole orange (cell-permeant) and propidium iodide (impermeable to healthy cells) as

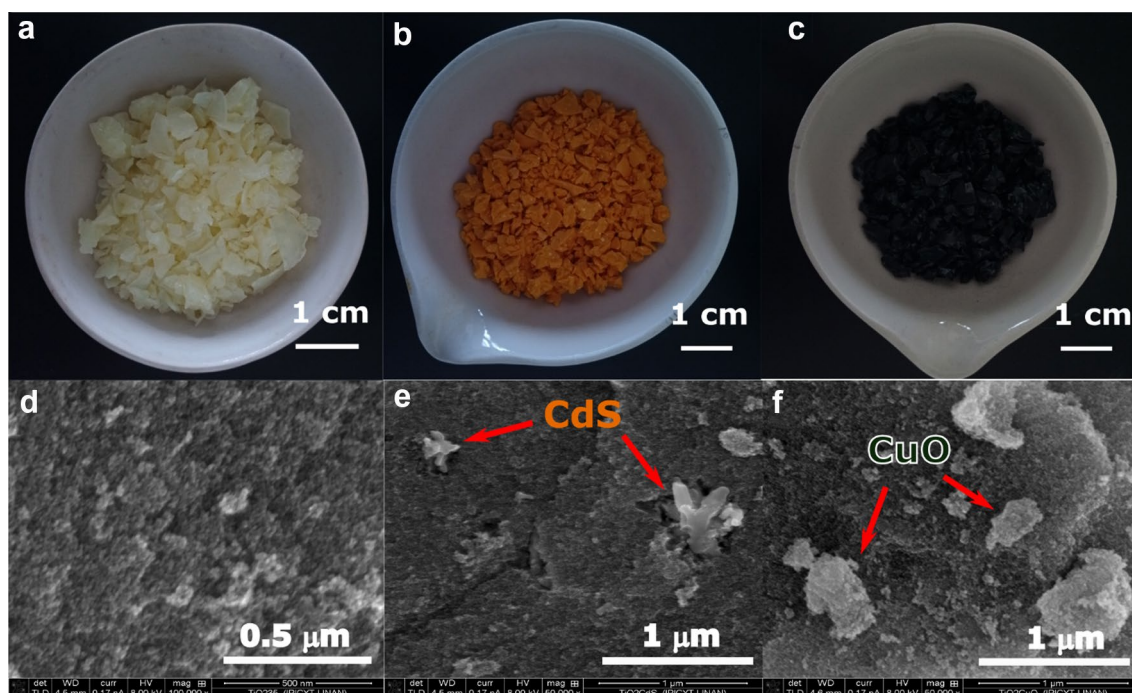


Fig. 4 Color and SEM images of m-TiO₂ **a, d**; m-TiO₂/CdS **b, e**; and m-TiO₂/CuO **c, f**

fluorochromes. In this work, bioaerosols inactivation are reported in terms of the percentage of living, dead, and injured cells. Also, throughout the text, the term cells or bacteria was used indistinctly.

3.2.1 Photolysis

The characterization of the influence in the viability of bioaerosols under blue LED light was performed. The residence time of the air flow in the empty reactor was 6 s, thus, each 30 min sampling is equivalent to 300 volumes of irradiated aerosols from the photoreactor, and samplings along 6 h of irradiation were taken. The results, presented in Fig. 5, show that < 35% of dead and injured cells were identified during the photolysis stage. Compared to the maximum dead and injured cells released by the biofilter solely (29.1%), it represents around 6% of inactivation. This slight inactivation could be produced because the photocatalytic system reached a maximum temperature of 42 °C, although high temperatures can produce bacterial mitigation, it is not enough to kill the most bacteria in a short time of exposure [55, 56]. Another factor to take into account for this variation in the percentage of dead and injured cells is that total cells at hour 6 were 6.1×10^8 cells/m³ which could influence the distribution of bioaerosols, and also, coincided with the maximum inactivation of bioaerosols. Considering these results, the percentage of living cells can fluctuate up to a minimum of 65% due to photolysis and bioaerosol loading.

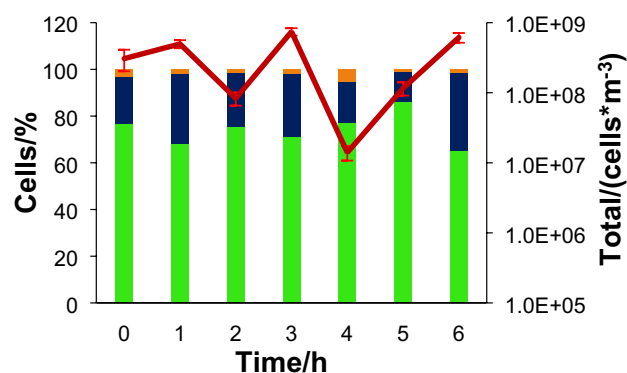


Fig. 5 Cell distribution of the photoreactor outlet in the photolysis process. Living cells (green bars), dead cells (blue bars), injured cells (orange bars). The solid line is the total cells with standard deviations (secondary axis)

If that percentage is lower, it can be attributed to a catalyst effect.

3.2.2 Photocatalysis 1st Cycle

Before the irradiation of blue light, the adsorption stage was performed for 24 h to ensure the saturation of active sites. The results of cell distribution during the adsorption and photocatalysis stage are shown in Fig. 6. The zero hour refers to the end of the adsorption stage (after 24 h) and the

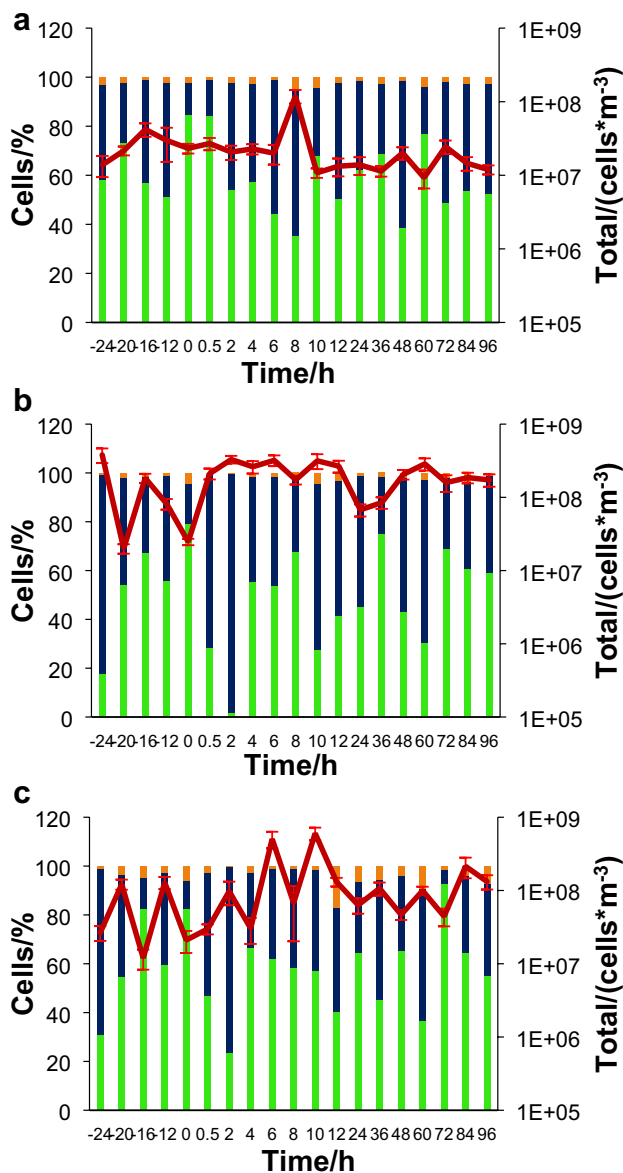


Fig. 6 Bioaerosols distribution of the photoreactor outlet when is irradiated with blue light (First cycle). **a** m-TiO₂, **b** m-TiO₂/CdS, and **c** m-TiO₂/CuO. Living cells (green bars), dead cells (blue bars), injured cells (orange bars). The solid line is the total cells with standard deviations (secondary axis)

start of photocatalytic activity. For m-TiO₂, the minimum percentage of living cells was reached after 12 h of adsorption (51.3%), whereas for m-TiO₂/CuO and m-TiO₂/CdS the minimum percentage of living cells was obtained at the minute 30 and corresponded to values of 30.7% and 17.9%, respectively. After 24 h of adsorption, the living cell percentages were 84.8%, 79.3%, and 82.8% for TiO₂, m-TiO₂/CdS, and m-TiO₂/CuO, respectively. All systems showed a maximum emission of living cells > 79% indicating the complete saturation of monoliths with bioaerosols.

For the photocatalytic stage, the first hours showed the high inactivation of bioaerosols. The m-TiO₂ had a minimum of 35.2% living cells at 8 h. In the case of m-TiO₂/CuO and m-TiO₂/CdS, this minimum appeared at hour 2 of photoreaction resulting in 23.5% and 0.1% of living cells, respectively. In all cases, after this first maximal inactivation, the percentage of living cells reaching a local maximum and subsequent local minimum. Three minima can be noted along the photocatalytic performance for the three systems at hours 8, 12, and 48 for m-TiO₂; at hours 2, 10, and 60 for m-TiO₂/CdS; and at hours 2, 12, and 60 for m-TiO₂/CuO. This cyclic behavior of bioaerosol inactivation can be due to a three-step process involved: adsorption, photocatalysis, and desorption. At the beginning of the photocatalytic activity, the adsorption stage of 24 h ensures the maximum load of bioaerosols on active sites, but as it degrades the cells, new bioaerosols were not available on the surface immediately and photocatalytic inactivation was not achieved until new bioaerosols were adsorbed [57]. This is an important challenge in photocatalytic reaction in continuous air flow because lower flow can improve the adsorption process but affect the mass diffusion slowing down the process significantly [58], in this way, high pressures could be explored.

As expected, the lower inactivation of bioaerosols was given for the system using m-TiO₂, this can be explained because the bandgap of pure anatase is 3.1 eV, and the main radiation used in this work was 2.7 eV. Thus, there is no absorption of electromagnetic radiation to produce free radicals on the surface of m-TiO₂, and the inactivation can be attributed to abrasion on the rough surface by the adsorption–desorption process commonly occurred in the dark stage for all monoliths [59, 60]. On the contrary, the impregnation of CdS (bandgap 2.2) and CuO (bandgap 1.4) nanoparticles ensures that irradiation was absorbed, and pairs of electron–holes were promoted. This type-II heterojunction systems improved the photocatalytic activity, thus, TiO₂ not only acted as support but also provided a delocalization of the photogenerated charge carriers [61].

After 96 h of photocatalytic performance, the change of a brown-yellow color in m-TiO₂ was evident (Fig S4). This change in the appearance of the impregnated monoliths (TiO₂/CdS, and m-TiO₂/CuO) was not noticed due to its predominant innate coloring. In all cases, the gravimetric analysis showed retention after the photocatalytic process of 7.2%, 2.0%, and 2.6% of organic compounds for m-TiO₂, m-TiO₂/CdS, and m-TiO₂/CuO, respectively. The organic compounds retained by the porous matrix are most likely bacterial residues (lipids, proteins, DNA). Although, the adsorption of toluene traces should not be discarded, which can interfere with the inactivation process. The high retention of organic matter in m-TiO₂ could be attributed to the low photocatalytic performance, where the bioaerosols

adsorbed were not degraded. In contrast, m-TiO₂/CdS and m-TiO₂/CuO degraded bioaerosols to more simple compounds allowing a better mass exchange.

In order to investigate the inactivation process on the surface of monoliths, the adhesion and morphology of adhered bioaerosols were analyzed. Figure 7 shows SEM images of bacteria found before and after the photocatalytic process. According to the shape of bacteria, the airborne cells were identified as bacilliform bacteria, in concordance with previous studies using activated sludge [62, 63]. Figures 7 (a, c, f) show bioaerosols adsorbed on mesoporous monoliths after 24 h of air flow in dark conditions. During this adsorption process, the shape of the bacterium was preserved with a range size between 1.0 to 2.5 μm. Figures 7 (b, d, e) show bioaerosols after the photocatalytic stage, in all samples the collapse of the rod-shaped structure was evident. This damage on the cellular membrane implied that the genetic material was exposed and the identification of dead cells by flow cytometry was adequate. Thus, the inactivation of bacteria in the photocatalytic process consists of 3 principal steps as shown in Fig. 8. The first step corresponds to the cell adhesion (adsorption) of airborne bacteria on the surface of monoliths. The second stage is the photocatalytic inactivation through the lipid peroxidation caused by the free radicals ($\cdot\text{OH}$, $\cdot\text{O}_2\text{H}$, $\cdot\text{O}_2^-$) generated through electron transfer in the type II heterojunction, producing rupture of the cellular membrane and subsequent collapse and death of cells (advanced oxidation process). The third step is the release of inactivated bioaerosols to, once again, allow the adsorption of bioaerosols from the continuous air flow. This mechanism of inactivation caused by membrane collapse resulted in irreversible damage, being a much more effective

method than UV light inactivation which photoreactivation may occur [64, 65].

To discard the release of the catalyst during the photocatalytic process, a qualitative assay of Cd and Cu was performed in all samples of bioaerosols. According to the UV–vis spectra, no absorbance > 350 nm was recorded, implying the absence of CdS, CuO, or Ti(IV) species in the samples (Fig. S5). This ensures that the nanoparticles are strongly retained on the mesoporous monoliths and its use in continuous air flow photocatalytic processes can be harmless. Additionally, the UV–vis spectra show a peak of absorbance at 280 nm involving a large amount of proteins in the solution, which implies the previous destruction of the cell membrane causing the dissolution of the proteins in the PBS buffer.

3.2.3 Catalysts Recycle Capacity

The reactivation of photocatalysts was achieved by calcination at 400 °C, 2 h. The identical amount of each catalyst was placed in the photoreactor, and the adsorption for 24 h was performed before the photoreaction. Figure 9 shows the cell distribution along the photocatalytic process. For m-TiO₂, m-TiO₂/CdS, and m-TiO₂/CuO the minimum percentage of living cells was 47.8%, 43.6%, and 37.7% respectively, which is higher than the results in the first cycle. Two local maxima and minima are still observed for all systems along the 96 h of photocatalytic activity. Once again, m-TiO₂ causes minor bioaerosol inactivation. Although m-TiO₂/CdS was the best photocatalyst in the first cycle reaching 99.9% of inactivation, for the second cycle, m-TiO₂/CuO performs high inactivation with respect to other monoliths.

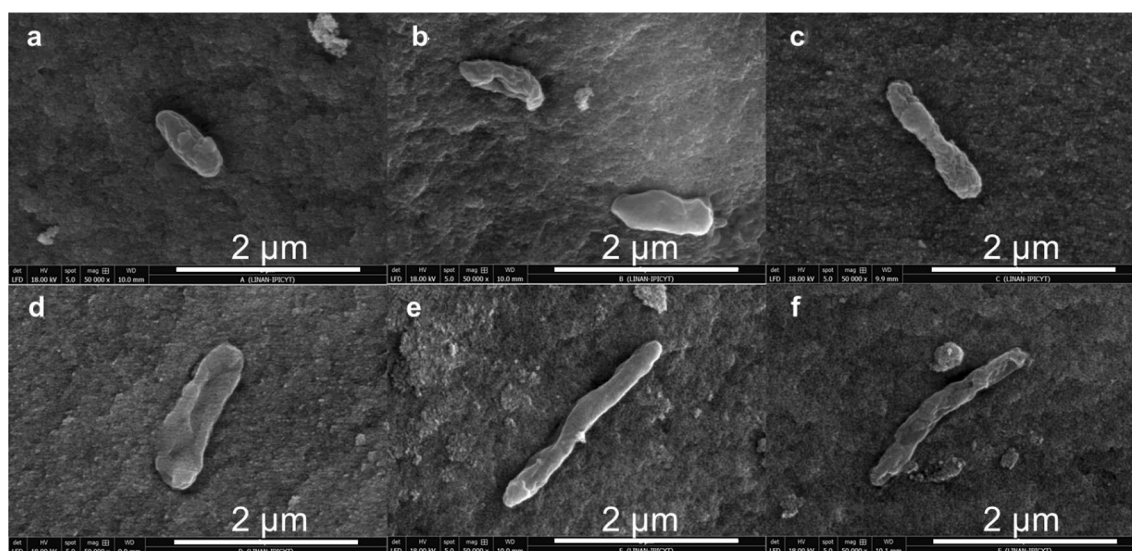


Fig. 7 SEM images of bioaerosols adsorbed on monoliths: **a, b** m-TiO₂/CdS; **c, d** m-TiO₂/CuO; and **e, f** m-TiO₂, before and after photocatalysis, respectively

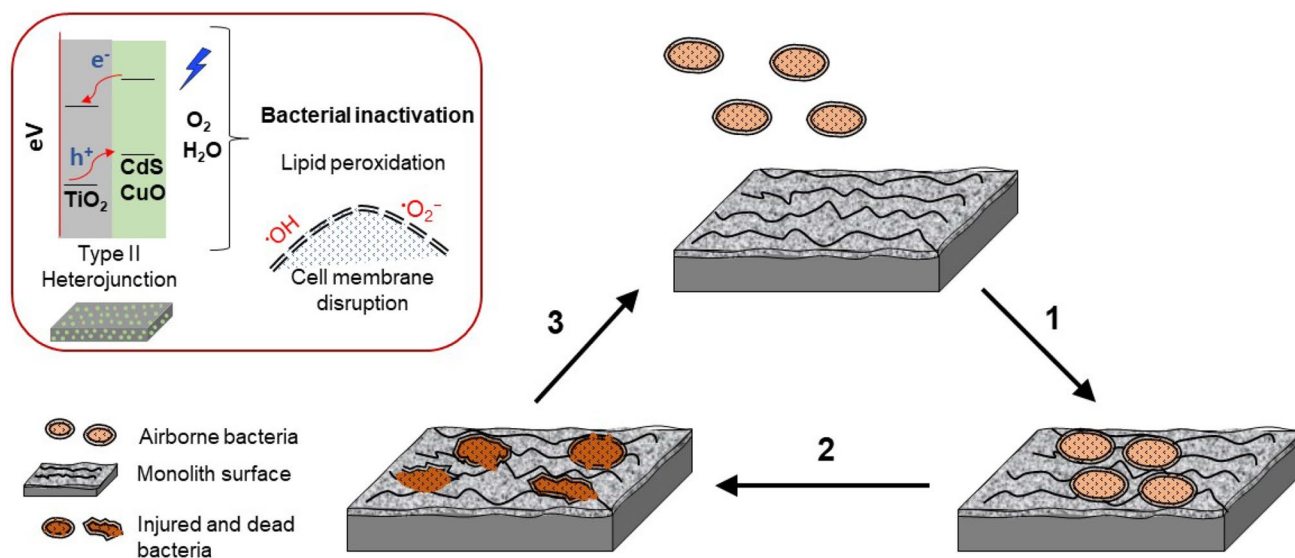


Fig. 8 Bioaerosol inactivation mechanism in the continuous flow photoreactor. **1** airborne bacteria are adsorbed on the monoliths. **2** photocatalysis produces reactive oxygen species affecting the adsorbed bacteria. **3** inactive bioaerosols are released, the monolith

surface becomes available to adsorb new airborne bacteria. Inset shows schematically the generation of reactive oxygen species from the monolith surface under blue light, causing lipid peroxidation

The inactivation of m-TiO₂/CuO was 62.3%, close to 75.5% in the first cycle, this result is probably due to the high specific surface area compared to the other monoliths (Table 1).

Variations in the total cell concentration through the inactivation performance in the first and second cycles are presented in Table 2. For m-TiO₂ the average cell concentration in the first cycle was 2.5×10^7 cells/m³, whereas in the second cycle the average concentration was 1.2×10^8 cells/m³. These results showed a difference of one order of magnitude which can be attributed to the retention of bacteria by adsorption, in accordance with the gravimetric analysis discussed above. On the contrary, for m-TiO₂/CdS and m-TiO₂/CuO, cell concentration in both photocatalytic cycles were practically equivalents, with a slightly higher load for the m-TiO₂/CdS system.

As can be seen in Table 2, there was not a significant influence of cell concentration on inactivation efficiency. However, it is important to remark that in catalytic reactions, high bioaerosol concentrations can be unsuitable due to the saturation of active sites [58]. Thus, considering that the concentration of bacteria in indoor air is between 10^5 – 10^6 cells/m³ lower than the studied in this work, the photocatalytic systems tested herein guarantee the complete treatment of a common load of bioaerosols in indoor air [66]. Unfortunately, the detection limit of flow cytometry is still an issue to resolve during the characterization of diluted samples of bioaerosols [67].

Once again, reactivation at 400 °C was performed to test a 3rd photocatalytic cycle. In this case, the three systems showed practically an insignificant effect of inactivation. In the third cycle of photocatalysis, m-TiO₂/CdS was able to release 34.0% and 2.7% of dead and injured cells respectively, maintaining a percentage of living cells superior to 63% which was similar to the percentage of living cells in the inlet flow of the photoreactor. m-TiO₂/CuO monolith performance was analogous, the maximum percentage of dead and injured cells released in the third cycle of photocatalysis was 40.6% and 2.6%, respectively. In this stage, the dead and injured cells population were closed to photolysis samples (~65% of living cells), thus, the photocatalytic activity was insignificant.

The loss of activity of catalysts in the 3rd cycle was probably related to the physicochemical changes when the monoliths are reactivated by calcination as discussed below. After two reactivations of catalysts by calcination at 400 °C, the adsorption capacity diminished because of the mesostructure sintering. For m-TiO₂ the specific surface area diminished to 86 m²/g and the pore diameter increased to 14.4 nm. Likewise, the pore size of impregnated monoliths m-TiO₂/CdS and m-TiO₂/CuO increased to 11.8 and 11.2 nm, respectively. Furthermore, the loss of hydroxyl groups on the mesoporous surface can influence the photocatalytic activity [68], in the case of gas-phase reactions the rehydroxylation of catalysts was not achieved due to the low humidity

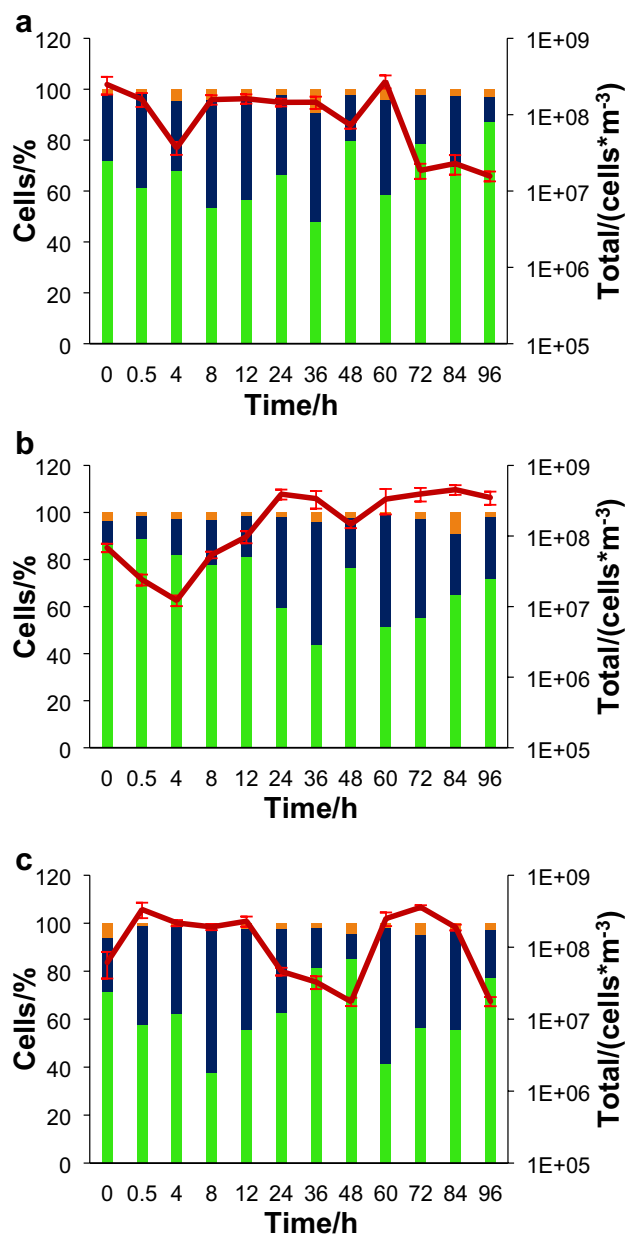


Fig. 9 Percentage of dead and injured cells after 2nd photocatalysis cycle. **a** m-TiO₂, **b** m-TiO₂/CdS, and **c** m-TiO₂/CuO. Living cells (green bars), dead cells (blue bars), injured cells (orange bars). The solid line is the total cells with standard deviations (secondary axis)

[69]. The bandgap of m-TiO₂/CdS and m-TiO₂/CuO after the 3rd reactivation remained practically unchanged (Fig. S6), which reinforces the hypothesis that surface physicochemical modifications are responsible directly for bioaerosol inactivation capacity. Thus, hydration steps previous and after the calcination should be useful to test that hypothesis. Despite the limited reusability of these materials, it is important to remark that the TiO₂ monoliths can be dissolved and used for new synthesis or applications [70].

In overall terms, the kinetics of adsorption of the pollutant on the active sites is a key factor to improve the activity of photocatalysts. Unfortunately, the high diversity of bioaerosols in common places requires multiple physicochemical surfaces. Studies on the influence of the surface charge or acid–base active sites to determine the most important factors that influence the AOP for bioaerosols inactivation remain necessary for the optimal design of photocatalysts.

4 Conclusions

The synthesis of monoliths of TiO₂ and impregnation with CdS and CuO nanoparticles was achieved using a one-pot methodology. The impregnated monoliths offered a high specific surface area (~100 m²/g) without the loss of nanoparticles under continuous air flow systems. The photocatalytic performance of monoliths m-TiO₂, m-TiO₂/CdS, and m-TiO₂/CuO showed a maximum bacteria inactivation of 64.8%, 99.9%, and 76.5%, respectively. The percentage of dead bacteria in bioaerosol samples was detected by flow cytometry and the membrane collapse caused by lipid peroxidation was observed by SEM. A cyclic inactivation behavior along 96 h of photocatalytic performance was noted, suggesting a three-step process limited by the adsorption–desorption stages. The catalysts maintained their photocatalytic activity until 2 cycles. In the third cycle of reuse, changes in mesoporous structure and possibly loss of hydroxyl groups during the reactivation by calcination hampered the adsorption and photocatalytic inactivation of bioaerosols. Thus, the adsorption of pollutants on the catalysts and their physicochemical structure is an important feature

Table 2 Cell concentration and percentage of inactivation in the photocatalytic experiments

Name	1st cycle		Maximum inactivation (%)	2nd cycle		Maximum inactivation (%)
	Bacteria concentration (x10 ⁷ cells/m ³)	Average (cells/m ³)		Bacteria concentration (x10 ⁷ cells/m ³)	Average (cells/m ³)	
m-TiO ₂	0.9–12	2.4 × 10 ⁷	64.8	1.6–27	1.2 × 10 ⁸	52.2
m-TiO ₂ /CdS	2.5–33	2.2 × 10 ⁸	99.9	1.2–45	2.2 × 10 ⁸	56.4
m-TiO ₂ /CuO	2.1–60	1.5 × 10 ⁸	75.5	1.8–36	1.6 × 10 ⁸	62.3

to improve the efficiency of inactivation in continuous flow photocatalysis.

Supplementary Information The online version contains supplementary material available at <https://doi.org/10.1007/s10562-021-03659-9>.

Acknowledgements A.H.G. acknowledges the postdoctoral fellowship from CONACYT (741134). Financial support for this work was managed by the CONACYT project (CB-2014-01-239622). The authors want to thank IPICYT for the use of its facilities, Laboratorio de Nuevos Materiales y Catálisis Heterogénea Ambiental-LANOCAT, Dr. Elizabeth Isaacs Páez (DCA), M.Sc. Ana Iris Peña Maldonado (LINAN) and Dr. Alejandro de las Peñas (DBM). Thank you to all health workers across the world who are fighting the COVID-19 pandemic.

Declarations

Conflict of interest No potential competing interest was reported by the authors.

References

- Ouyang X et al (2019) Environmental regulation, economic growth and air pollution: Panel threshold analysis for OECD countries. *Sci Total Environ* 657:234–241
- Kampa M, Castanas E (2008) Human health effects of air pollution. *Environ Pollut* 151(2):362–367
- Mitova, M.I., et al., *Human chemical signature: Investigation on the influence of human presence and selected activities on concentrations of airborne constituents*. Environmental Pollution, 2020. **257**.
- Tian Y, Yao X, Chen L (2019) Analysis of spatial and seasonal distributions of air pollutants by incorporating urban morphological characteristics. *Comput Environ Urban Syst* 75:35–48
- Carazo Fernández L et al (2013) Indoor air contaminants and their impact on respiratory pathologies. *Archivos de Bronconeumología (English Edition)* 49(1):22–27
- Ghosh B, Lal H, Srivastava A (2015) Review of bioaerosols in indoor environment with special reference to sampling, analysis and control mechanisms. *Environ Int* 85:254–272
- Morawska, L., et al., *How can airborne transmission of COVID-19 indoors be minimised?* Environment International, 2020. **142**.
- Chu DK et al (2020) Physical distancing, face masks, and eye protection to prevent person-to-person transmission of SARS-CoV-2 and COVID-19: a systematic review and meta-analysis. *The Lancet* 395(10242):1973–1987
- An, T., H. Zhao, and P.K. Wong, *Advances in Photocatalytic Disinfection*. Green Chemistry and Sustainable Technology. 2017.
- Dalrymple OK et al (2010) A review of the mechanisms and modeling of photocatalytic disinfection. *Appl Catal B* 98(1–2):27–38
- Rodríguez-González, V., et al., *An approach to the photocatalytic mechanism in the TiO₂-nanomaterials microorganism interface for the control of infectious processes*. Applied Catalysis B: Environmental, 2020. **270**.
- Helali, S., et al., *Solar photocatalysis: A green technology for E. coli contaminated water disinfection. Effect of concentration and different types of suspended catalyst*. Journal of Photochemistry and Photobiology A: Chemistry, 2014. **276**: 31–40.
- Mousset E, Dionysiou DD (2020) Photoelectrochemical reactors for treatment of water and wastewater: a review. *Environ Chem Lett* 18(4):1301–1318
- Negron A et al (2020) Using flow cytometry and light-induced fluorescence to characterize the variability and characteristics of bioaerosols in springtime in Metro Atlanta, Georgia. *Atmos Chem Phys* 20(3):1817–1838
- Xu Z et al (2011) Bioaerosol science, technology, and engineering: past, present, and future. *Aerosol Sci Technol* 45(11):1337–1349
- Sengupta A et al (2005) Bioaerosol characterization by surface-enhanced Raman spectroscopy (SERS). *J Aerosol Sci* 36(5–6):651–664
- Rodrigues-Silva C et al (2016) Bacteria and fungi inactivation by photocatalysis under UVA irradiation: liquid and gas phase. *Environ Sci Pollut Res* 24(7):6372–6381
- Doss, N., et al., *Photocatalytic Decontamination of Airborne T2 Bacteriophage Viruses in a Small-Size TiO₂/β-SiC Alveolar Foam LED Reactor*. Water, Air, & Soil Pollution, 2018. **229**(2).
- Li, P., et al., *Metal-organic frameworks with photocatalytic bactericidal activity for integrated air cleaning*. Nature Communications, 2019. **10**(1).
- Danilenko, I., et al., *Photocatalytic Composite Nanomaterial and Engineering Solution for Inactivation of Airborne Bacteria*. Topics in Catalysis, 2020.
- Jiang Q, Ding C, Liu Y (2018) A type of novel glass for indoor air cleaning under visible-light. *Build Environ* 137:226–234
- Daikoku T et al (2015) Decomposition of organic chemicals in the air and inactivation of aerosol-associated influenza infectivity by photocatalysis. *Aerosol and Air Quality Research* 15(4):1469–1484
- Sompalli, N.K., et al., *Mesoporous monolith designs of mixed phased titania codoped Sm³⁺/Er³⁺ composites: A super responsive visible light photocatalysts for organic pollutant clean-up*. Applied Surface Science, 2020. **504**.
- Gogoi N et al (2018) TiO₂ supported gold nanoparticles: An efficient photocatalyst for oxidation of alcohol to aldehyde and ketone in presence of visible light irradiation. *Chem Phys Lett* 692:224–231
- Kim J, Jang J (2018) Inactivation of airborne viruses using vacuum ultraviolet photocatalysis for a flow-through indoor air purifier with short irradiation time. *Aerosol Sci Technol* 52(5):557–566
- Ola, O. and M. Mercedes Maroto-Valer, *Copper based TiO₂ honeycomb monoliths for CO₂ photoreduction*. Catal. Sci. Technol., 2014. **4**(6): p. 1631–1637.
- Zhong L, Haghight F (2015) Competitive Adsorption Behaviour of Binary Mixtures on Titanium Dioxide. *The Canadian Journal of Chemical Engineering* 93(9):1657–1666
- Tsang CHA et al (2019) Titanium oxide based photocatalytic materials development and their role of in the air pollutants degradation: Overview and forecast. *Environ Int* 125:200–228
- Boscaro P et al (2019) C, N-doped TiO₂ monoliths with hierarchical macro-/mesoporosity for water treatment under visible light. *Microporous Mesoporous Mater* 280:37–45
- Deshmane VG et al (2015) Mesoporous nanocrystalline TiO₂ supported metal (Cu, Co, Ni, Pd, Zn, and Sn) catalysts: Effect of metal-support interactions on steam reforming of methanol. *J Mol Catal A: Chem* 408:202–213
- Hsieh B-J et al (2017) Tuning metal support interactions enhances the activity and durability of TiO₂-supported Pt nanocatalysts. *Electrochim Acta* 224:452–459
- Yang G et al (2013) One-step solvothermal synthesis of hierarchically porous nanostructured CdS/TiO₂ heterojunction with higher visible light photocatalytic activity. *Appl Surf Sci* 283:402–410
- Yu H, Irie H, Hashimoto K (2010) Conduction Band Energy Level Control of Titanium Dioxide: Toward an Efficient Visible-Light-Sensitive Photocatalyst. *J Am Chem Soc* 132(20):6898–6899

34. Wang M et al (2018) Construction of TiO₂/CdS heterojunction photocatalysts with enhanced visible light activity. *Appl Surf Sci* 455:729–735
35. Al-Fahdi T et al (2019) Visible light active CdS@TiO₂ core-shell nanostructures for the photodegradation of chlorophenols. *J Photochem Photobiol, A* 374:75–83
36. Abidi, M., et al., *Photocatalytic indoor/outdoor air treatment and bacterial inactivation on CuO/TiO₂ prepared by HiPIMS on polyester cloth under low intensity visible light*. *Applied Catalysis B: Environmental*, 2019. **259**.
37. Moon, E.W., et al., *Photocatalytic inactivation of viral particles of human norovirus by Cu-doped TiO₂ non-woven fabric under UVA-LED wavelengths*. *Science of The Total Environment*, 2020. **749**.
38. Zheng X et al (2017) Electrospinning Cu–TiO₂ nanofibers used for photocatalytic disinfection of bacteriophage f2: preparation, optimization and characterization. *RSC Adv* 7(82):52172–52179
39. Zhong L, Haghight F (2018) Modeling of by-products from photocatalytic oxidation (PCO) indoor air purifiers: A case study of ethanol. *Build Environ* 144:427–436
40. Malayeri, M., et al., *Modeling of gas-phase heterogeneous photocatalytic oxidation reactor in the presence of mass transfer limitation and axial dispersion*. *Chemical Engineering Journal*, 2020. **386**.
41. Valdez-Castillo M, Saucedo-Lucero JO, Arriaga S (2019) Photocatalytic inactivation of airborne microorganisms in continuous flow using perlite-supported ZnO and TiO₂. *Chem Eng J* 374:914–923
42. Chen, P.-S. and C.-S. Li, *Bioaerosol characterization by flow cytometry with fluorochrome*. *Journal of Environmental Monitoring*, 2005. **7**(10).
43. Hasegawa G et al (2010) Facile Preparation of Hierarchically Porous TiO₂ Monoliths. *J Am Ceram Soc* 93(10):3110–3115
44. Wang Z et al (2020) Step-scheme CdS/TiO₂ nanocomposite hollow microsphere with enhanced photocatalytic CO₂ reduction activity. *J Mater Sci Technol* 56:143–150
45. Dhineshbabu NR et al (2015) Study of structural and optical properties of cupric oxide nanoparticles. *Appl Nanosci* 6(6):933–939
46. Li J et al (2018) Extinction coefficient per CdE (E = Se or S) unit for zinc-blende CdE nanocrystals. *Nano Res* 11(8):3991–4004
47. Ojeda-López R et al (2015) SBA-15 materials: calcination temperature influence on textural properties and total silanol ratio. *Adsorption* 21(8):659–669
48. Hernández-Gordillo A, Campero A, Vera-Robles LI (2018) Mesoporous TiO₂ synthesis using a semi-hard biological template. *Microporous Mesoporous Mater* 270:140–148
49. Huang J et al (2006) Synthesis and characterization of CuO/TiO₂ catalysts for low-temperature CO oxidation. *Catal Commun* 7(12):1029–1034
50. Wang G et al (2012) Enhanced photocatalytic activity of powders (P25) via calcination treatment. *Int J Photoenergy* 2012:1–9
51. Shi Q et al (2019) CuO/TiO₂ heterojunction composites: an efficient photocatalyst for selective oxidation of methanol to methyl formate. *Journal of Materials Chemistry A* 7(5):2253–2260
52. Li B et al (2017) A multifunctional noble-metal-free catalyst of CuO/TiO₂ hybrid nanofibers. *Appl Catal A* 531:1–12
53. Uma K et al (2020) Enhanced photocatalytic activity of CdS nanostar decorated SiO₂/TiO₂ composite spheres and the simulation effect using FDTD model. *Ionics* 27(1):397–406
54. Hu, X.-R., et al., *A short review of bioaerosol emissions from gas bioreactors: Health threats, influencing factors and control technologies*. *Chemosphere*, 2020. **253**.
55. Jung JH, Lee JE, Kim SS (2009) Thermal effects on bacterial bioaerosols in continuous air flow. *Sci Total Environ* 407(16):4723–4730
56. Ricker EB et al (2018) Thermal shock susceptibility and regrowth of *Pseudomonas aeruginosa* biofilms. *Int J Hyperth* 34(2):168–176
57. Bouzaza A, Vallet C, Laplanche A (2006) Photocatalytic degradation of some VOCs in the gas phase using an annular flow reactor. *J Photochem Photobiol, A* 177(2–3):212–217
58. Schreck M, Niederberger M (2019) Photocatalytic gas phase reactions. *Chem Mater* 31(3):597–618
59. Ciston S, Lueptow RM, Gray KA (2008) Bacterial attachment on reactive ceramic ultrafiltration membranes. *J Membr Sci* 320(1–2):101–107
60. Rtimi, S., et al., *Effect of surface pretreatment of TiO₂ films on interfacial processes leading to bacterial inactivation in the dark and under light irradiation*. *Interface Focus*, 2015. **5**(1).
61. Gao P et al (2012) Hierarchical TiO₂/CdS “spindle-like” composite with high photodegradation and antibacterial capability under visible light irradiation. *J Hazard Mater* 229–230:209–216
62. Valenzuela-Reyes E et al (2014) Performance and bacterial population composition of an n-hexane degrading biofilter working under fluctuating conditions. *Appl Biochem Biotechnol* 174(2):832–844
63. Covarrubias-García I et al (2019) Effects of ozone treatment on performance and microbial community composition in biofiltration systems treating ethyl acetate vapours. *Chemosphere* 233:67–75
64. Oguma K, Katayama H, Ohgaki S (2002) Photoreactivation of *Escherichia coli* after low- or medium-pressure UV disinfection determined by an endonuclease sensitive site assay. *Appl Environ Microbiol* 68(12):6029–6035
65. Guo M-T, Kong C (2019) Antibiotic resistant bacteria survived from UV disinfection: Safety concerns on genes dissemination. *Chemosphere* 224:827–832
66. Górny RL (2020) Microbial aerosols: sources, properties, health effects, exposure assessment—a review. *Kona Powder Part J* 37:64–84
67. Ou F et al (2017) Absolute bacterial cell enumeration using flow cytometry. *J Appl Microbiol* 123(2):464–477
68. Oosawa, Y. and M. Grätzel, *Effect of surface hydroxyl density on photocatalytic oxygen generation in aqueous TiO₂ suspensions*. *Journal of the Chemical Society, Faraday Transactions 1: Physical Chemistry in Condensed Phases*, 1988. **84**(1).
69. Nanayakkara CE, Larish WA, Grassian VH (2014) Titanium Dioxide Nanoparticle Surface Reactivity with Atmospheric Gases, CO₂, SO₂, and NO₂: Roles of Surface Hydroxyl Groups and Adsorbed Water in the Formation and Stability of Adsorbed Products. *The Journal of Physical Chemistry C* 118(40):23011–23021
70. Mukherjee A, Raichur AM, Modak JM (2005) Dissolution studies on TiO₂ with organics. *Chemosphere* 61(4):585–588

Publisher's Note Springer Nature remains neutral with regard to jurisdictional claims in published maps and institutional affiliations.